


## Article

# Structure, Microstructure and Magnetocaloric/Thermomagnetic Properties at the Early Sintering of MnFe(P,Si,B) Compounds

Tvirgyn Qianbai, Hargen Yibole and Francois Guillou \* 

College of Physics and Electronic Information, Inner Mongolia Key Laboratory for Physics and Chemistry of Functional Materials, Inner Mongolia Normal University, 81 Zhaowuda Rd., Hohhot 010022, China; 20214016026@mails.imnu.edu.cn (T.Q.); hyibole@imnu.edu.cn (H.Y.)

\* Correspondence: francoisguillou@imnu.edu.cn

**Abstract:** Minimizing the sintering time while ensuring high performances is an important optimization step for the preparation of magnetocaloric or thermomagnetic materials produced by powder metallurgy. Here, we study the influence of sintering time on the properties of a  $\text{Mn}_{0.95}\text{Fe}_1\text{P}_{0.56}\text{Si}_{0.39}\text{B}_{0.05}$  compound. In contrast to former reports investigating different annealing temperatures during heat treatments of several hours or days, we pay special attention to the earliest stages of sintering. After ball-milling and powder compaction, 2 min sintering at 1100 °C is found sufficient to form the desired  $\text{Fe}_2\text{P}$ -type phase. Increasing the sintering time leads to a sharper first-order magnetic transition, a stronger latent heat, and usually to a larger isothermal entropy change, though not in all cases. As demonstrated by DSC or magnetization measurements, these parameters present dissimilar time evolutions, highlighting the existence of various underlying mechanisms. Chemical inhomogeneities are likely responsible for broadened transitions for the shortest sinterings. The development of strong latent heat requires longer sinterings than those for sharpening the magnetic transition. The microstructure may play a role as the average grain size progressively increases with the sintering time from 3.5  $\mu\text{m}$  (2 min) to 30.1  $\mu\text{m}$  (100 h). This systematic study has practical consequences for optimizing the preparation of MnFe(P,Si,B) compounds, but also raises intriguing questions on the influence of the microstructure and of the chemical homogeneity on magnetocaloric or thermomagnetic performances.



**Citation:** Qianbai, T.; Yibole, H.; Guillou, F. Structure, Microstructure and Magnetocaloric/Thermomagnetic Properties at the Early Sintering of MnFe(P,Si,B) Compounds. *Metals* **2024**, *14*, 385. <https://doi.org/10.3390/met14040385>

Academic Editors: Victorino Franco, João Horta Belo and Luis Miguel Moreno-Ramírez

Received: 14 February 2024  
Revised: 20 March 2024  
Accepted: 25 March 2024  
Published: 26 March 2024



**Copyright:** © 2024 by the authors. Licensee MDPI, Basel, Switzerland. This article is an open access article distributed under the terms and conditions of the Creative Commons Attribution (CC BY) license (<https://creativecommons.org/licenses/by/4.0/>).

**Keywords:** magnetocaloric effect; thermomagnetic materials; powder metallurgy; magnetic properties; phase transitions

## 1. Introduction

Applying a magnetic field change on a magnetocaloric material induces an isothermal magnetic entropy change ( $\Delta S$ ) or and adiabatic temperature change ( $\Delta T_{ad}$ ) that can be used for magnetic refrigeration or heat pumps [1–5]. Reciprocally, applying a temperature change on a thermomagnetic material will trigger a change in magnetization or magnetic induction in the presence of an external magnetic field, which may be used to recover waste heat into work or electricity [6–10]. Both magnetocaloric and thermomagnetic applications present some environmental advantages, making them highly desirable for magnetic refrigeration, magnetic heat pumping or recovering waste heat into electricity or work. For applications near room temperature, promising magnetocaloric/thermomagnetic materials families include  $\text{Gd}_5(\text{Si,Ge})_4$  [11],  $\text{La}(\text{Fe,Si})_{13}$  and its hydrides [12,13], Heusler alloys [14], MnCoGe- or MnNiGe-based compounds [15,16]. Compounds deriving from  $\text{Fe}_2\text{P}$  such as MnFe(P,As) [17], MnFe(P,Si) [18] or MnFe(P,Si,B) [19] are also appealing as they combine giant magnetocaloric/thermomagnetic effects at their first-order ferromagnetic transition with a high tunability of the Curie temperature. Magnetocaloric applications can also be considered over an extended range of temperature; so, magnetocaloric properties have been systematically investigated in various other material systems, including oxides [20–22], transition metals, and rare earth intermetallic systems [23–29].

Magnetocaloric performances are generally controlled by intrinsic properties of the material which are primarily given by its chemical composition, e.g., the saturation magnetization, the magnetic transition temperature, the heat capacity, or the Erhenfest order of the transition (presence of a latent heat). In some cases, sample preparation may also strongly influence the magnetocaloric effect. Setting aside the case of micro- or nano-structured materials which involve specific mechanisms [30–32] and going beyond the simple aspect of sample purity or secondary phase content, the sample synthesis technique may exert an extrinsic control on the phase transition and therefore significantly affect the magnetocaloric performances. One of the most typical examples is the great sensitivity of martensitic transitions to microstructural details [33–38].

Magnetocaloric compounds deriving from  $\text{Fe}_2\text{P}$  are based on a first-order ferromagnetic transition without a change in crystal symmetry or a significant volume change. Opposite discontinuities on  $a$  and  $c$  axes, however, result in an increase in the  $c/a$  ratio of about +2% from the ferromagnetic to the paramagnetic state [19]. These local mechanical strains are a coupling mechanism for the magnetic transition and can be anticipated to interact with microstructural defects (secondary phase, porosity, microcracks, etc.). As a result, different preparation techniques yielding various microstructures lead to dissimilar magnetic properties for a given composition and affect the magnetocaloric performances. Various methods have been investigated to prepare  $\text{Fe}_2\text{P}$ -type  $\text{MnFe}(\text{P,Si})$  and  $\text{MnFe}(\text{P,Si,B})$  magnetocaloric materials including drop synthesis [39], casting [40], arc-melting [41], melt-spinning [42], and single crystal [43] methods. Yet, until now, a solid-state synthesis after a ball-milling stage remains the most widely used and that yielding among the highest magnetocaloric performances [44]. Systematic investigations on the effect of the sintering temperature and sintering duration have been carried out to optimize the magnetocaloric effect (mostly the isothermal entropy change) in  $\text{Mn}_{1.000}\text{Fe}_{0.950}\text{P}_{0.595}\text{Si}_{0.330}\text{B}_{0.075}$  [45],  $\text{MnFe}_{0.95}\text{P}_{0.587}\text{Si}_{0.34}\text{B}_{0.073}$  [46] or the sample purity in  $(\text{Fe,Co})_2(\text{P,Si})$  [47] compounds. They indicated that sintering for about 24 h at 1100 °C ending by quenching in room-temperature water is recommended to avoid the formation secondary phases and to maximize the performances. Yet, such long sintering is not desired for industrial production and would require careful optimization. In addition, these former studies paid attention to relatively long sintering, of several hours or even days. To draw a clearer picture of the phase formation of magnetocaloric/thermomagnetic  $\text{MnFe}(\text{P,Si,B})$  compounds, an investigation of the earliest stages of the solid-state reaction is needed. Here, we select one  $\text{MnFe}(\text{P,Si,B})$  composition presenting a first-order ferromagnetic transition with a Curie temperature slightly above room temperature (thermomagnetic applications are targeted), and investigate the structural, microstructural and magnetic properties as a function of the sintering time. This extensive experimental study covering sintering from 2 min to 100 h reveals dissimilar characteristic times for the phase formation, the microstructural evolution and the development of high latent heat and a sharp magnetic transition. Contrary to popular belief, it is observed that longer sintering does not always result in a larger isothermal entropy change. A phenomenological model is proposed to explain it and the possible underlying reasons are discussed.

## 2. Materials and Methods

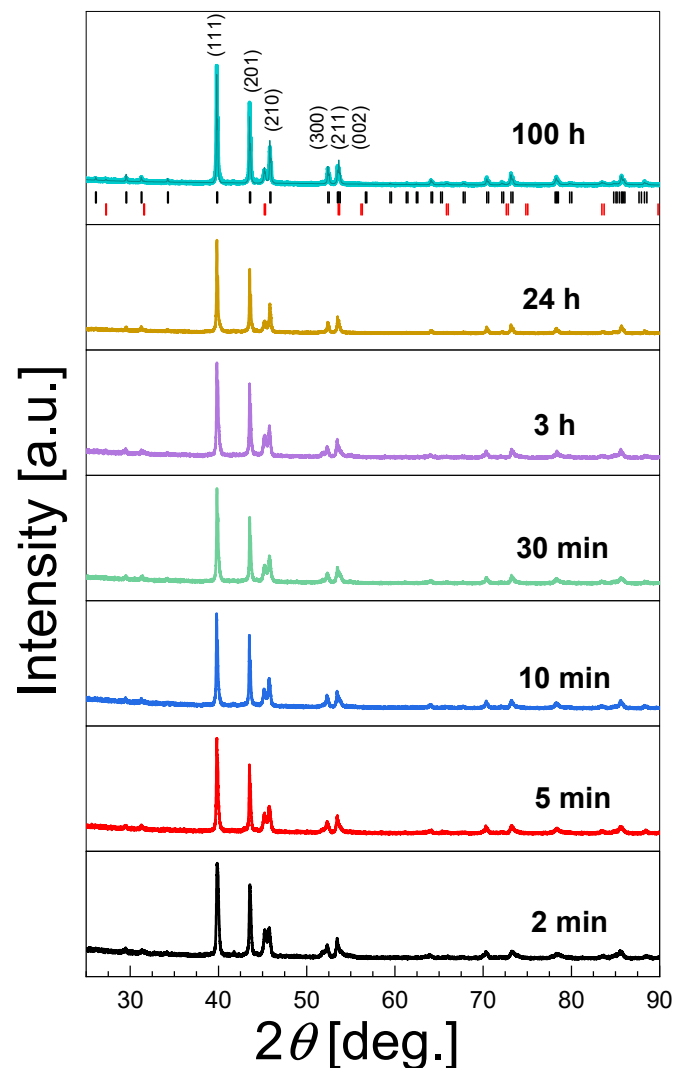
A batch of  $\text{Mn}_{0.95}\text{FeP}_{0.56}\text{Si}_{0.39}\text{B}_{0.05}$  was prepared by ball-milling elemental starting materials, Mn (99.9%) chips, Fe (99.9%) powder, P (97.3%) powder, Si (99.999%) lumps, and B (99.9%) pieces using a ball/sample mass ratio of 5:1 at 360 rpm for 10 h. The resulting powder was then compacted into cylinders of about 2.5 g/piece using a uniaxial pressure of 750 MPa. The samples were then sealed in quartz tubes backfilled with 200 mbar argon gas. A vertical furnace, pre-heated at 1100 °C, was used for sintering the samples (hot insertion) during 2 min, 5 min, 10 min, 30 min, 3 h, 24 h and 100 h prior to quenching the samples in room temperature water. A sintering temperature of 1100 °C was selected as it was found to be the optimal sintering temperature during former studies [45–47].

Powder X-ray diffraction was carried out on an Empyrean PANalytical diffractometer in the  $2\theta$  range of 20–90°. The Rietveld method, as implemented in the FullProf software (version: April 2019), was used for crystal structure refinement and evaluation of the secondary phase content [48]. The surface morphology was investigated using Hitachi SU8010 and TM3030Plus electron microscopes equipped with energy-dispersive X-ray EDX spectroscopy (performed at 15 keV). The surface of the bulk samples was prepared by polishing using sandpaper down to 2000 grit, and then using diamond pastes from 16  $\mu\text{m}$  to 2  $\mu\text{m}$  spread on a polishing cloth. The MIPAR software (version: 3.4.0.2) was used for quantitative analysis of SEM images [49]. The magnetization was measured on bulk pieces of about 20 mg using a vibrating sample magnetometer installed on a VersaLab Quantum Design system. Isofield magnetization curves were recorded in sweep mode at 1 K  $\text{min}^{-1}$  (no thermal lag correction). Calorimetry measurements were performed on a TA Instruments DSC 2500 at 5 K  $\text{min}^{-1}$  using a liquid nitrogen cooler, He, as the exchange gas and standard aluminum pans.

### 3. Results

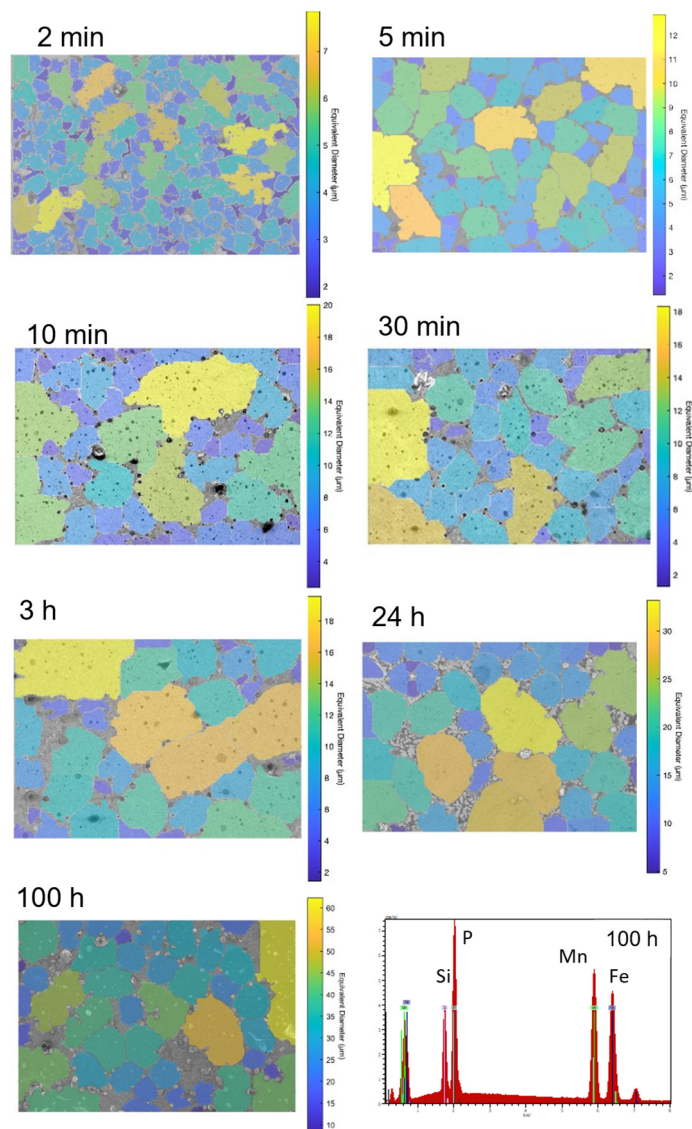
Figure 1 presents the powder XRD patterns for  $\text{Mn}_{0.95}\text{FeP}_{0.56}\text{Si}_{0.39}\text{B}_{0.05}$  samples sintered for different durations. It is found that a very short sintering of 2 min is sufficient to form the desired product with an  $\text{Fe}_2\text{P}$ -type structure (hexagonal space group  $P\bar{6}2m$ ). As found in studies based on much longer sintering times [45,46], an additional peak at about 45.3° characteristically marks out the presence of a cubic secondary phase with a 3:1 metal/metalloid ratio and close to  $(\text{Mn,Fe})_3\text{Si}$  in composition ((220) Bragg position of the cubic secondary phase). Increasing the sintering time does not significantly affect the peak position of the main phase. The peak shape of the main phase is somewhat broadened for the shortest sintering but quickly sharpens with increasing the sintering time. Higher main phase content, better crystallinity and better chemical homogeneity are likely involved in the increased intensity for the XRD peak of the main phase when increasing the sintering time. The relative intensity of the secondary phase peak appears to decrease with increasing the sintering time from about 11 wt% for 2 min down to about 7 wt% for 100 h of sintering.

Figure 2 illustrates the surface of polycrystalline samples sintered for different durations. Only a selection is presented, but about 10 pictures per samples were analyzed to obtain a quantitative estimate of the average grain size. As usually observed in this material family, there is a significant porosity and a few inclusions of  $\text{SiO}_2$ . The secondary phase content is mostly located at intergranular spacings. Local chemical analyses by energy-dispersive spectroscopy in SEM confirm that the secondary phase presents a metal/metalloid ratio of 3:1. Electron dispersive spectroscopy (EDX) in SEM yields an effective elemental concentration for the main phase in sample sintered for 100 h of  $\text{Mn}_{34.11\pm 1.1}\text{Fe}_{34.78\pm 1.2}\text{P}_{20.34\pm 0.5}\text{Si}_{10.77\pm 0.3}$ . In comparison to the nominal composition,  $\text{Mn}_{32.76}\text{Fe}_{34.48}\text{P}_{19.31}\text{Si}_{13.45}$ , not accounting for boron which cannot be resolved in SEM/EDX, the formation of a secondary phase whose composition is close to  $\text{MnFe}_2\text{Si}$  leads to a Si deficiency of the main phase and a slight increase in Mn and P contents. Similar observations were made for the samples with shorter sintering. EDX measurements did not indicate a significant compositional difference between the various grains of the main phase, even for the shortest sintering. If chemical inhomogeneities are present between the grains of the main phase, they are either weaker than the compositional accuracy of the EDX system, typically a few mol%, or spread in a size smaller than the investigated micrometric scale. Looking at the microstructure as a function of the sintering duration, a clear grain size growth is observed, from an average grain size of about 3.5  $\mu\text{m}$  for 2 min to 30.1  $\mu\text{m}$  for 100 h of sintering.



**Figure 1.** Powder XRD patterns measured at room temperature for  $\text{Mn}_{0.95}\text{FeP}_{0.56}\text{Si}_{0.39}\text{B}_{0.05}$  samples with different sintering durations. The top panel with the sample sintered for 100 h illustrates the refinement process, observed intensity (thicker line), calculated intensity (thinner line), Bragg positions for the  $\text{Fe}_2\text{P}$ -type phase (upper set of vertical lines) and for the  $\text{MnFe}_2\text{Si}$  phase (lower set of vertical lines). For clarity, only the observed intensity is displayed for the other samples.

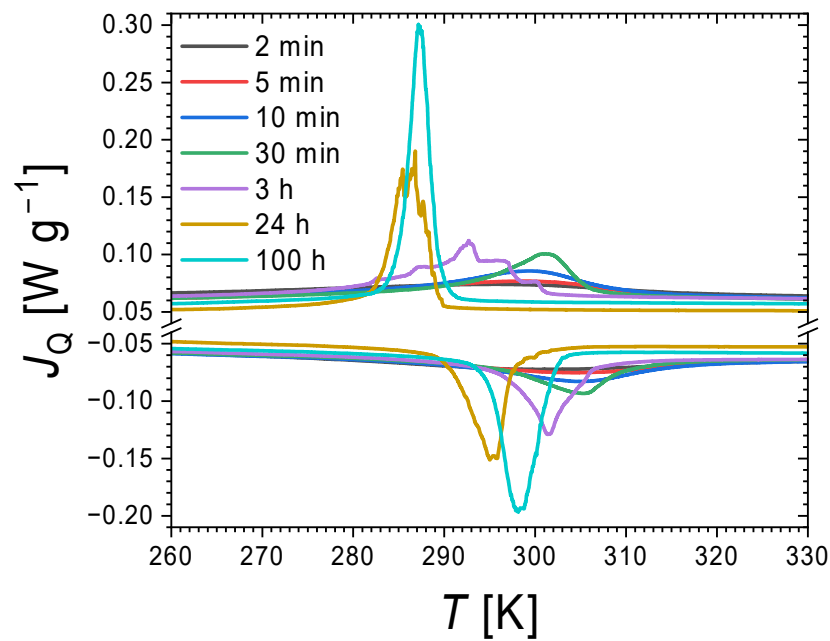
Differential scanning calorimetry (DSC) measurements for  $\text{Mn}_{0.95}\text{FeP}_{0.56}\text{Si}_{0.39}\text{B}_{0.05}$  samples sintered for different durations are presented in Figure 3. All samples show a thermal anomaly marking their magnetic transition in the temperature range from  $\sim 297$  to  $\sim 306$  K upon heating. Some samples show a decomposition of the latent heat ( $L$ ) peak into individual thermal events upon cooling. We believe this feature being observed in the samples with the strongest transitions (longer sinterings) should not be interpreted as a distribution of transition temperatures in the sample, but rather as the expression of burst-like kinetic aspects of the transition. The samples with the shortest sintering (10 min and less) show particularly broad and weak peaks, yet they still present a finite thermal hysteresis. Increasing the sintering time leads to a progressive growth and sharpening of the latent peaks. The strongest latent heat peak is observed for the sample sintered for 100 h. The thermal hysteresis appears to increase with the sintering duration and strengthening of the latent heat peak, from about 4 K for the sample sintered for 2 min up to about 8 K for the sample sintered for 100 h. One should, however, recall that dynamic techniques such as DSC measurements tend to overestimate the thermal hysteresis due to thermal lags; so, the thermal hysteresis may actually be smaller.



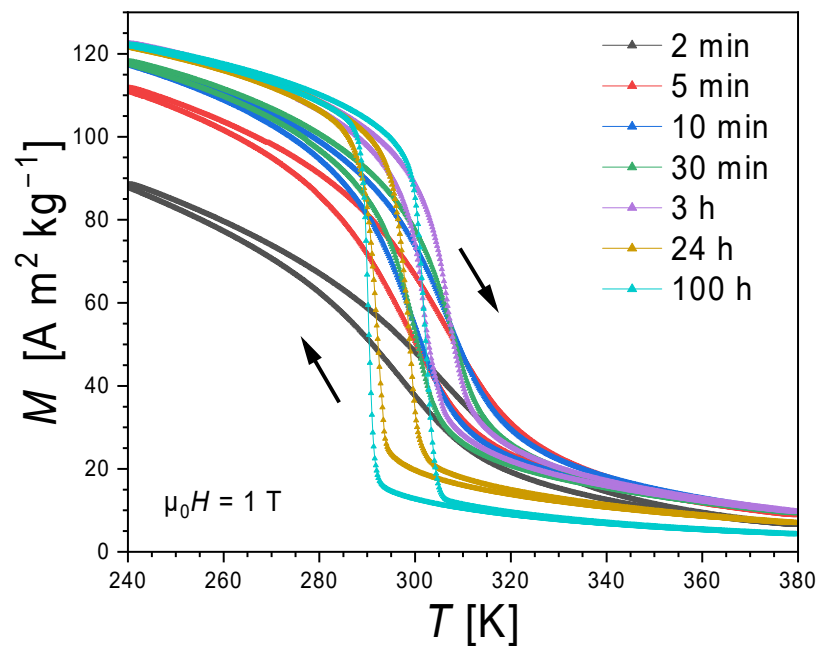
**Figure 2.** SEM images of  $\text{Mn}_{0.95}\text{FeP}_{0.56}\text{Si}_{0.39}\text{B}_{0.05}$  samples sintered at  $1100\text{ }^{\circ}\text{C}$  for different durations. A color code highlighting the equivalent diameter of each grain is superposed on the images. Bottom right: EDX spectrum of the main phase for the  $\text{Mn}_{0.95}\text{FeP}_{0.56}\text{Si}_{0.39}\text{B}_{0.05}$  sample sintered at  $1100\text{ }^{\circ}\text{C}$  for 100 h.

Figure 4 presents isofield magnetization curves upon heating and cooling in an external field of  $\mu_0 H = 1\text{ T}$ . As expected for such a composition and in agreement with DSC data, all samples show a ferromagnetic transition with a finite thermal hysteresis, from  $\sim 7\text{ K}$  for 2 min up to  $\sim 10\text{ K}$  for 100 h of sintering. The transition temperatures upon heating are spread between 299 K and 308 K without direct correlation with the sintering duration. The sharpness of the transition, however, presents a clear and systematic evolution. The transition sharpens with the increase in sintering time. Most pronounced between 2 min to 10 min sintering, the transition continues to become sharper with increasing the sintering time. From 24 h to 100 h of sintering, the sharpness no longer evolves; however, the transition becomes noticeably more hysteretic.





**Figure 3.** DSC measurements upon cooling (upper set of curves) and heating (lower set of curves) for  $\text{Mn}_{0.95}\text{FeP}_{0.56}\text{Si}_{0.39}\text{B}_{0.05}$  samples sintered for different durations.



**Figure 4.** Isofield magnetization measurements of  $\text{Mn}_{0.95}\text{FeP}_{0.56}\text{Si}_{0.39}\text{B}_{0.05}$  samples sintered for different durations. Heating (higher transition temperatures) and cooling (lower transition temperatures) curves are shown for each sample.

A set of isofield magnetization measurements were carried out while increasing the applied magnetic field for the samples sintered from 5 min to 100 h, see Figure 5. The shift of the transition temperature ( $T_{tr}$ ) due to the field  $dT_{tr}/\mu_0 dH$  ranges from 3.0 to 3.6  $\text{K T}^{-1}$  for the different samples. All samples present a progressive, yet limited, broadening of the transition with the increase in the magnetic field. The broadening of the  $M(T)$  curves induced by high magnetic fields does not appear more pronounced for the 5 min and 10 min samples than that for the samples with longer sintering. This is fairly surprising

in view of the particularly small thermal anomaly observed in DSC measurements. This suggests that the weak thermal anomaly on DSC for the shortest sinterings cannot be interpreted as a second-order transition, since the latter would have resulted in a strong broadening when increasing the magnetic field. For samples sintered for a short time, one is still in the presence of a first-order magnetic transition, but with a distribution of transition temperatures over an extended temperature range due to chemical disorder. The finite thermal hysteresis and a shift  $dT_{tr}/\mu_0 dH$  of the overall distribution remains comparable to that observed in samples with a sharper transition.

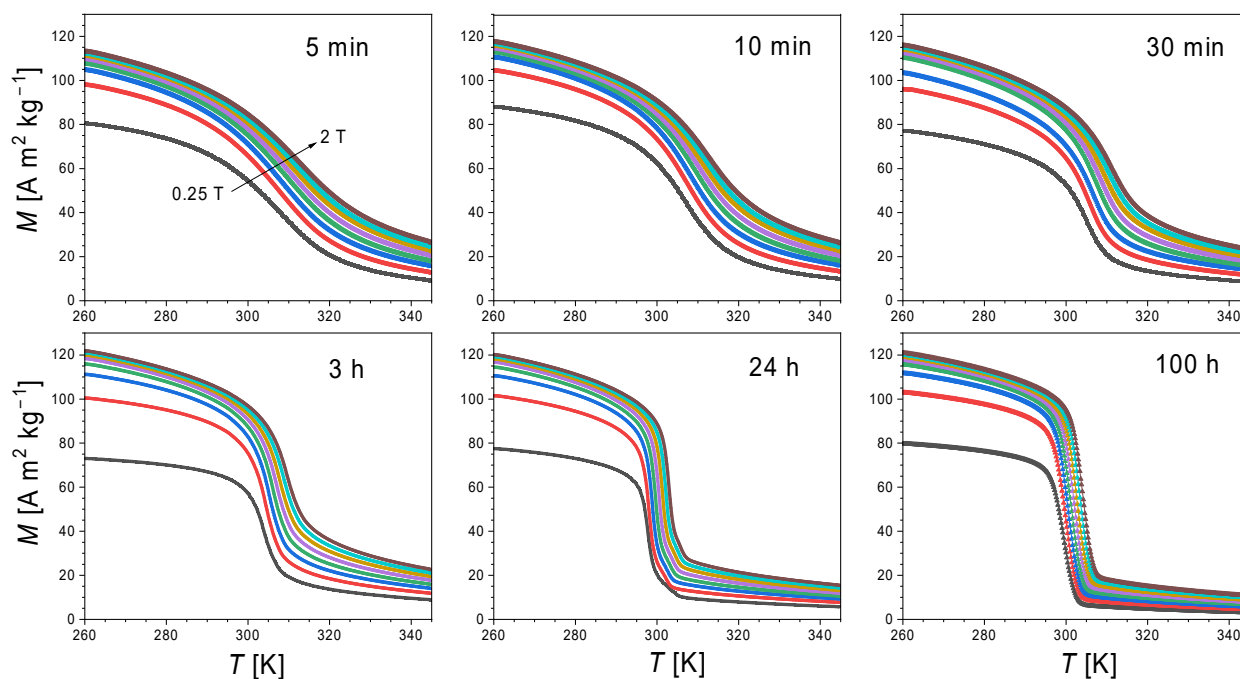


**Figure 5.** Isofield magnetization curves recorded upon heating in increasing applied magnetic fields from 0.25 T to 2 T in 0.25 T increment for  $\text{Mn}_{0.95}\text{FeP}_{0.56}\text{Si}_{0.39}\text{B}_{0.05}$  samples sintered for different durations.

The isothermal entropy change ( $\Delta S$ ) calculated from heating isofield  $M(T)$  data is presented in Figure 6 for different sintering durations. We note that calculating  $\Delta S$  from a set of  $M(T)$  curves allows us to avoid the “spike” artefact which usually occurs when  $\Delta S$  is indirectly determined from isothermal magnetization  $M(H)$  curves at first-order magnetic transitions [50]. Generally, increasing the sintering time sharpens the  $\Delta S$  peak and leads to an increase in  $\Delta S$  maximum. One, however, observes that the largest  $\Delta S$  maximum in  $\mu_0 H = 1$  T is reached for 24 h of sintering, while in 2 T, it is reached for 100 h of sintering. This opposite tendency illustrates the not-so-trivial influence of the synthesis conditions on caloric performances. Increasing the sintering time sharpens the transition and therefore increases the  $\Delta S$ , but the field range where the  $\Delta S$  saturates, i.e., when the latent heat is fully induced by the field, is reached for a lower magnetic field (case of 24 h of sintering in 2 T). On the other hand, longer sintering also results in stronger latent heat, offering the possibility to reach larger  $\Delta S$  but also requiring a larger magnetic field to fully induce the first-order transition by applying a magnetic field (case of 100 h of sintering in 2 T).

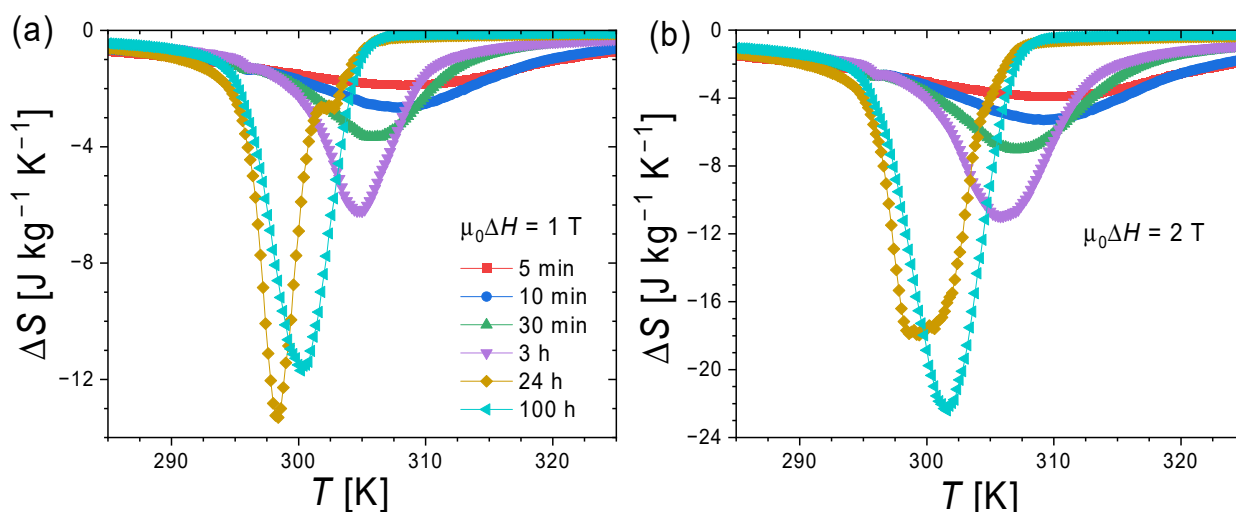


**Figure 6.** Isothermal entropy change calculated from heating isofield  $M(T)$  data for  $\text{Mn}_{0.95}\text{FeP}_{0.56}\text{Si}_{0.39}\text{B}_{0.05}$  samples sintered over different durations in applied field of 1 T (a) and 2 T (b).

To illustrate the non-similar influence that transition broadening and latent heat have on the magnetocaloric performances and on the  $\Delta S$  maximum in particular, we simulate the  $\Delta S$  maximum by using a simplified latent heat model for the giant magnetocaloric effect [51–53]. Within this framework allowing for parametric investigations, the high field  $\Delta S$  is field independent and purely originates from the latent heat of the transition leading to  $\Delta S = L/T_{\text{tr}}$ . Below a critical saturation field,  $B^* = L\delta T_{\text{tr}}/(T_{\text{tr}}|\Delta M|)$ , where  $\delta T_{\text{tr}}$  is the width of the transition and  $\Delta M$  the discontinuity in magnetization,  $\Delta S$  is field dependent and amounts to  $\Delta S = (\mu_0 H |\Delta M|)/\delta T_{\text{tr}}$ . Starting from parameters somewhat reflecting the observed properties,  $\Delta M = 70 \text{ A m}^2 \text{ kg}^{-1}$ ,  $\delta T_{\text{tr}} = 6 \text{ K}$  (approximately twice the full width at half maximum from  $M(T)$  curves),  $L = 6 \text{ J g}^{-1}$ , and  $T_{\text{tr}} = 310 \text{ K}$ , we investigate the effect of decreasing the transition width or increasing the latent heat, see Figure 7. Decreasing the transition width would not affect the  $\Delta S$  at high field but would allow us to reach a larger  $\Delta S$  in the field-dependent regime. On the other hand, increasing the latent heat does not affect the field-dependent range, but increases the achievable  $\Delta S$  at high magnetic fields.

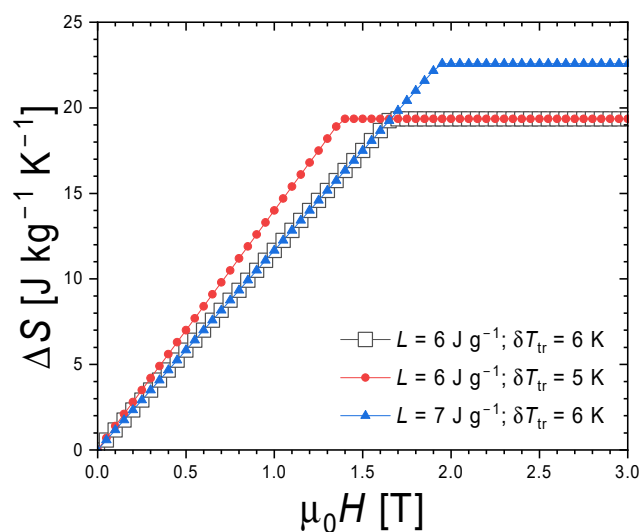


**Figure 7.** Simulated  $\Delta S$  maximum from a latent heat model considering three sets of input parameters.



#### 4. Discussion

The dependence of a few selected properties on the sintering duration is summarized in Figure 8. All parameters present a somewhat similar behavior with a fast evolution at the beginning of sintering, typically during the first 30 min, followed by a slower evolution, in some cases spread until 100 h. One can, however, note some specific differences.

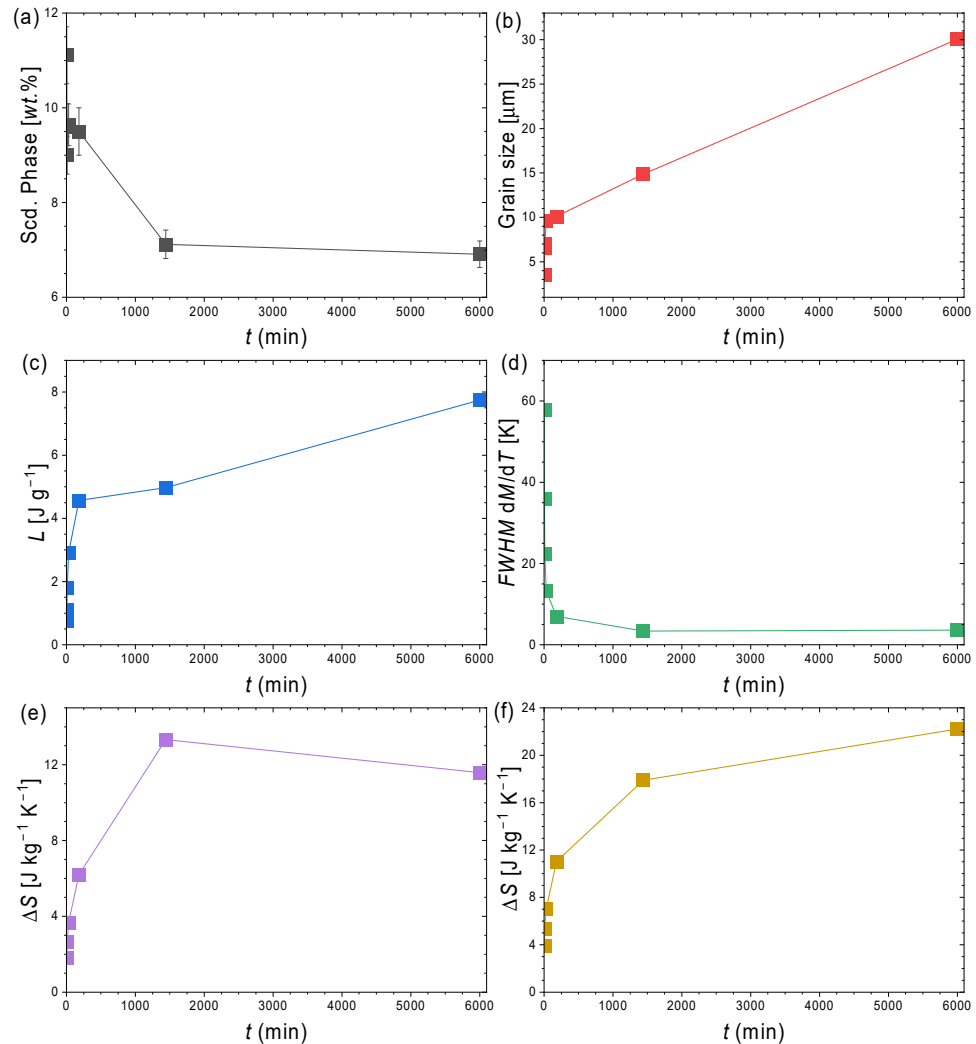


**Figure 8.** Sintering time dependence for  $\text{Mn}_{0.95}\text{FeP}_{0.56}\text{Si}_{0.39}\text{B}_{0.05}$  compound of: (a) the secondary phase content estimated from refinement of powder XRD; (b) average grain size (equivalent diameter) from analysis of SEM pictures (5–10 pictures analyzed per sample); (c) latent heat from DSC measurements upon heating (integration from 288 to 323 K using a linear background); (d) full width at half maximum of the temperature derivative of  $M(T)$  curves (FWHM of the  $dM/dT(T)$  peak) recorded upon heating in 1 T; (e) maximum of the isothermal entropy change upon heating in 1 T; (f) idem as (e) but in a 2 T field.

The secondary phase content presents a rather limited reduction, from ~11 wt% to ~7 wt%, taking place over relatively large time windows. In contrast, the other parameters present evolutions that are much larger in amplitude: a factor ~7 increase in the grain size, a factor ~8 increase in latent heat, a factor ~20 decrease in the width of the ferromagnetic transition, and a factor ~6 increase in the  $\Delta S$  maximum. This forms a first indication that the elimination of the secondary phase is only a minor contribution to the increase in  $\Delta S$  by increasing the sintering time. The limited evolution of the secondary phase content is also in line with the rather limited spread of the Curie temperatures between the different

samples. A Si-rich (Mn,Fe)<sub>3</sub>Si secondary phase usually leads to a Si depletion in the main phase (see EDX measurements), which, in turn, results in decreased Curie temperatures (typical-8 K/Si atom%). Here, the Curie temperatures remain within ~10 K for the different samples, which is well in line with only minor deviations in the average secondary phase content.

The overall time dependence of the grain size is akin to the common power law for normal grain growth kinetic, where  $D-D_0 = Kt^{1/n}$ , with  $D$  is the average grain size,  $D_0$  the initial grain size,  $K$  a material constant and  $n$  the grain growth exponent [54]. A  $\ln(D)$  vs.  $\ln(t)$  plot (not shown) presents a relatively linear dependence (linear regression factor  $R^2 \approx 0.90$ ) and yields an exponent  $n = 4.2 \pm 0.6$ . This value differs from two, indicating that multiple driving forces play a part in the grain growth of these multicomponent samples. Interestingly, the grain growth remains important even from 24 h to 100 h of sintering. We can also note that the latent heat presents a time evolution very similar to the grain size. This suggests that large grains favor stronger first-order transitions. This observation is actually in line with a former study on particle size reduction (top-down approach, opposite to the present study), where the strongest transitions and largest thermal hysteresis were found in the largest particles [55].

The width of the magnetic transition presents an intriguing shape evoking an exponential decay  $Ae^{-t/\tau}$ , with  $t$  being the sintering time,  $\tau$  a time constant and  $A$  a pre-factor. A fit of the experimental data yields a time constant  $\tau \sim 7$  min. Among the various parameters, the width of the transition is the one showing the fastest evolution, with most of its change takes place during the first 30 min of sintering, and it does not show a significant evolution from 24 h to 100 h of sintering (one actually observes a very limited broadening at 100 h). It is likely that the primary mechanism influencing the broadening of the magnetic transition is the chemical homogeneity which is driven by solid-state diffusion. Long ball-milling (10 h) yields relatively homogeneous powders, which, when followed by a solid-state reaction at a relatively high temperature (1100 °C corresponding to approximately 90% of the melting temperature), can lead to a sharp transition within a rather limited sintering time.

One observes that the  $\Delta S$  maximum follows its own sintering duration dependence, with a rather slow evolution compared to the other parameters. For 1 T, it increases for the first 3 h, but still presents a significant evolution from 3 to 24 h, ending through a decrease from 24 to 100 h. In 2 T, the  $\Delta S$  maximum shows a continuous increase from 24 h to 100 h of sintering. Figure 7 illustrates the complex relationship that the  $\Delta S$  maximum shares with other parameters. Both the sharpening of the magnetic transition and the increase in latent heat favor an increase in  $\Delta S$  maximum, but their effects are dependent on the considered applied magnetic field. A sharp magnetic transition will be most crucial to observe large  $\Delta S$  at intermediate field changes, whereas high latent heat sets a condition on the largest achievable  $\Delta S$  at high magnetic fields. As the sintering duration affects transition broadening and latent heat in a non-similar manner,  $\Delta S$  presents a unique evolution as a function of the sintering duration for each considered magnetic field change. The decrease in  $\Delta S$  maximum at 1 T from 24 h to 100 h of sintering is likely ascribable to the slightly broader transition for 100 h of sintering. In contrast, the increase in  $\Delta S$  maximum at 2 T from 24 h to 100 h of sintering originates from a stronger latent heat. For magnetic fields larger than the 2 T presently investigated, it is likely that the influence of latent heat will become even more pronounced.

In practice, when working with thermomagnetic applications primarily requiring a sharp transition and large  $dM/dT$  at intermediate magnetic fields (typically in 1 T or less), relatively short sintering of 30 min to 3 h would be sufficient. On the other hand, magnetocaloric applications require larger  $\Delta S$  in 1 T to 2 T, stronger latent heat, and therefore longer sintering of typically 24 h.

## 5. Conclusions

The influence of sintering duration on the properties of a  $\text{Mn}_{0.95}\text{FeP}_{0.56}\text{Si}_{0.39}\text{B}_{0.05}$  compound is investigated. It is found that 2 min sintering at 1100 °C is sufficient to form the desired  $\text{Fe}_2\text{P}$ -type product. Longer sintering is, however, required to optimize the magnetic and phase transition properties. A chemical homogenization of approximately 30 min is needed to obtain a sharp magnetic transition. Even longer sintering times are desirable to develop a strong latent heat. This study of the secondary phase content, grain size, latent heat, transition broadening and  $\Delta S$  in different magnetic fields as a function of the sintering duration reveals non-similar evolutions and the existence of different time scales. In practice, the sintering of  $\text{MnFe}(\text{P},\text{Si},\text{B})$  materials for thermomagnetic applications could be shorter than that for magnetocaloric ones. Sintering duration influences the transition broadening and latent heat, in turn affecting the maximal isothermal entropy change in a complex manner, but the actual underlying mechanisms remain challenging to address. Further investigations of the chemical homogeneity with an atomic resolution would be needed to disentangle the role played by chemical disorder and that of the microstructure in general.

**Author Contributions:** Conceptualization, T.Q. and F.G.; investigation, T.Q.; resources, F.G. and H.Y.; data curation, T.Q.; writing—original draft preparation, T.Q.; writing—review and editing, H.Y. and F.G.; supervision, F.G.; project administration, H.Y.; funding acquisition, H.Y. and F.G. All authors have read and agreed to the published version of the manuscript.

**Funding:** This research was funded by the Natural Science Foundation of China, grant numbers 52150610486 and 51961033 and by the Inner Mongolia Autonomous Region, grant number NJYT23107.

**Data Availability Statement:** The original contributions presented in the study are included in the article, and further inquiries can be directed to the corresponding author.

**Conflicts of Interest:** The authors declare no conflicts of interest.

## References

- Gschneidner, K.A., Jr.; Pecharsky, V.K.; Tsokol, A.O. Recent developments in magnetocaloric materials. *Rep. Prog. Phys.* **2005**, *68*, 1479–1539. [[CrossRef](#)]
- Gutfleisch, O.; Willard, M.A.; Brück, E.; Chen, C.H.; Sankar, S.G.; Liu, J.P. Magnetic Materials and Devices for the 21st Century: Stronger, Lighter, and More Energy Efficient. *Adv. Mater.* **2011**, *23*, 821–842. [[CrossRef](#)]
- Smith, A.; Bahl, C.R.H.; Bjørk, R.; Engelbrecht, K.; Nielsen, K.K.; Pryds, N. Materials Challenges for High Performance Magnetocaloric Refrigeration Devices. *Adv. Energy Mater.* **2012**, *2*, 1288–1318. [[CrossRef](#)]
- Kitanovski, A. Energy Applications of Magnetocaloric Materials. *Adv. Energy Mater.* **2020**, *10*, 1903741. [[CrossRef](#)]
- Law, J.Y.; Moreno-Ramírez, L.M.; Díaz-García, Á.; Franco, V. Current perspective in magnetocaloric materials research. *J. Appl. Phys.* **2023**, *133*, 040903. [[CrossRef](#)]
- Elliott, J.J. Thermomagnetic generator. *J. Appl. Phys.* **1959**, *30*, 1774. [[CrossRef](#)]
- Kishore, R.A.; Priya, S. A review on design and performance of thermomagnetic devices. *Renew. Sust. Energy Rev.* **2018**, *81*, 33–44. [[CrossRef](#)]
- Waske, A.; Dzekan, D.; Sellschopp, K.; Berger, D.; Stork, A.; Nielsch, K.; Fähler, S. Energy harvesting near room temperature using a thermomagnetic generator with a pretzel-like magnetic flux topology. *Nat. Energy* **2018**, *4*, 68–74. [[CrossRef](#)]
- Ahmed, R.; Jin, C.P.; Zeeshan; Mehmood, M.U.; Lim, S.H.; Lee, J.; Chun, W. Optimization of a cylindrical thermomagnetic engine for power generation from low-temperature heat sources. *Int. J. Energy Res.* **2021**, *45*, 8117–9712. [[CrossRef](#)]
- Ma, Z.; Chen, H.; Liu, X.L.; Xing, C.F.; Wu, M.L.; Wang, Y.X.; Liu, P.R.; Ou, Z.Q.; Shen, J.; Taskaev, S.V.; et al. Thermomagnetic Generation Performance of Gd and  $\text{La}(\text{Fe}, \text{Si})_{13}\text{H}_y/\text{In}$  Material for Low-Grade Waste Heat Recovery. *Adv. Sustain. Syst.* **2021**, *5*, 2000234. [[CrossRef](#)]
- Pecharsky, V.K.; Gschneidner, K.A., Jr. Giant magnetocaloric effect in  $\text{Gd}_5(\text{Si}_2\text{Ge}_2)$ . *Phys. Rev. Lett.* **1997**, *78*, 4494–4497. [[CrossRef](#)]
- Hu, F.X.; Shen, B.G.; Sun, J.R.; Cheng, Z.H.; Rao, G.H.; Zhang, X.X. Influence of negative lattice expansion and metamagnetic transition on magnetic entropy change in the compound  $\text{LaFe}_{11.4}\text{Si}_{1.6}$ . *Appl. Phys. Lett.* **2001**, *78*, 3675–3677. [[CrossRef](#)]
- Fujita, A.; Fujieda, S.; Hasegawa, Y.; Fukamichi, K. Itinerant-electron metamagnetic transition and large magnetocaloric effects in  $\text{La}(\text{Fe}_x\text{Si}_{1-x})_{13}$  compounds and their hydrides. *Phys. Rev. B* **2003**, *67*, 104416. [[CrossRef](#)]
- Planes, A.; Manosa, L.; Moya, X.; Krenke, T.; Acet, M.; Wassermann, E.F. Magnetocaloric effect in Heusler shape-memory alloys. *J. Magn. Magn. Mater.* **2007**, *310*, 2767–2769. [[CrossRef](#)]
- Trung, N.T.; Zhang, L.; Caron, L.; Buschow, K.H.J.; Brück, E. Giant magnetocaloric effects by tailoring the phase transitions. *Appl. Phys. Lett.* **2010**, *96*, 172504. [[CrossRef](#)]

16. Liu, E.; Wang, W.; Feng, L.; Zhu, W.; Li, G.; Chen, J.; Zhang, H.; Wu, G.; Jiang, C.; Xu, H.; et al. Stable magnetostructural coupling with tunable magnetoresponsive effects in hexagonal ferromagnets. *Nat. Commun.* **2012**, *3*, 873. [[CrossRef](#)] [[PubMed](#)]
17. Tegus, O.; Brück, E.; Buschow, K.H.J.; de Boer, F.R. Transition-metal-based magnetic refrigerants for room-temperature applications. *Nature* **2002**, *415*, 150–152. [[CrossRef](#)]
18. Dung, N.H.; Ou, Z.Q.; Caron, L.; Zhang, L.; Cam Thanh, D.T.; de Wijs, G.A.; de Groot, R.A.; Buschow, K.H.J.; Brück, E. Mixed magnetism for refrigeration and energy conversion. *Adv. Energy Mater.* **2011**, *1*, 1215–1219. [[CrossRef](#)]
19. Guillou, F.; Porcari, G.; Yibole, H.; van Dijk, N.; Brück, E. Taming the first-order transition in giant magnetocaloric materials. *Adv. Mater.* **2014**, *26*, 2671–2675. [[CrossRef](#)]
20. Phan, M.H.; Yu, S.C. Review of the magnetocaloric effect in manganite materials. *J. Magn. Magn. Mater.* **2007**, *308*, 325–340. [[CrossRef](#)]
21. Salazar-Muñoz, V.E.; Lobo Guerrero, A.; Palomares-Sánchez, S.A. Review of magnetocaloric properties in lanthanum manganites. *J. Magn. Magn. Mater.* **2022**, *562*, 169787. [[CrossRef](#)]
22. Pęczkowski, P.; Łuszczek, M.; Szostak, E.; Muniraju, N.K.C.; Krztoń-Maziop, A.; Gondek, Ł. Superconductivity and appearance of negative magnetocaloric effect in  $\text{Ba}_{1-x}\text{K}_x\text{BiO}_3$  perovskites, doped by Y, La and Pr. *Acta Mater.* **2022**, *222*, 117437. [[CrossRef](#)]
23. Radelytskyi, I.; Aleshkevych, P.; Gawryluk, D.J.; Berkowski, M.; Zajarniuk, T.; Szewczyk, A.; Gutowska, M.; Hawelek, L.; Włodarczyk, P.; Fink-Finowicki, J.; et al. Structural, magnetic, and magnetocaloric properties of  $\text{Fe}_7\text{Se}_8$  single crystals. *J. Appl. Phys.* **2018**, *124*, 143902. [[CrossRef](#)]
24. Ćwik, J.; Koshkid'ko, Y.; Nenkov, K.; Tereshina-Chitrova, E.; Małecka, M.; Weise, B.; Kowalska, K. Magnetocaloric performance of the three-component  $\text{Ho}_{1-x}\text{Er}_x\text{Ni}_2$  ( $x = 0.25, 0.5, 0.75$ ) Laves phases as composite refrigerants. *Sci. Rep.* **2022**, *12*, 12332. [[CrossRef](#)] [[PubMed](#)]
25. Politova, G.; Tereshina, I.; Ovchenkova, I.; Aleroev, A.R.; Koshkid'ko, Y.; Cwik, J.; Drulis, H. Investigation of Magnetocaloric Properties in the  $\text{TbCo}_2\text{-H}$  System. *Crystals* **2022**, *12*, 1783. [[CrossRef](#)]
26. Kamantsev, A.P.; Koshkid'ko, Y.S.; Gaifullin, R.Y.; Musabirov, I.I.; Koshelev, A.V.; Mashirov, A.V.; Sokolovskiy, V.V.; Buchelnikov, V.D.; Ćwik, J.; Shavrov, V.G. Inverse Magnetocaloric Effect in Heusler  $\text{Ni}_{44.4}\text{Mn}_{36.2}\text{Sn}_{14.9}\text{Cu}_{4.5}$  Alloy at Low Temperatures. *Metals* **2023**, *13*, 1985. [[CrossRef](#)]
27. Kutynia, K.; Przybył, A.; Gębara, P. The Effect of Substitution of Mn by Pd on the Structure and Thermomagnetic Properties of the  $\text{Mn}_{1-x}\text{Pd}_x\text{CoGe}$  Alloys (Where  $x = 0.03, 0.05, 0.07$  and  $0.1$ ). *Materials* **2023**, *16*, 5394. [[CrossRef](#)] [[PubMed](#)]
28. Salamatin, D.A.; Krasnorussky, V.N.; Magnitskaya, M.V.; Semeno, A.V.; Bokov, A.V.; Velichkov, A.; Surowiec, Z.; Tsvyashchenko, A.V. Some Magnetic Properties and Magnetocaloric Effects in the High-Temperature Antiferromagnet  $\text{YbCo}_2$ . *Magnetochemistry* **2023**, *9*, 152. [[CrossRef](#)]
29. Sikora, M.; Bajorek, A.; Chrobak, A.; Deniszczyk, J.; Ziółkowski, G.; Chełkowska, G. Effect of Ni Substitution on the Structural, Magnetic, and Electronic Structure Properties of  $\text{Gd}_{0.4}\text{Tb}_{0.6}(\text{Co}_{1-x}\text{Ni}_x)_2$  Compounds. *Int. J. Mol. Sci.* **2022**, *23*, 13182. [[CrossRef](#)]
30. Belo, J.H.; Pires, A.L.; Araújo, J.P.; Pereira, A.M. Magnetocaloric materials: From micro- to nanoscale. *J. Mater. Res.* **2019**, *34*, 134–157. [[CrossRef](#)]
31. Dudek, M.R.; Dudek, K.K.; Wolak, W.; Wojciechowski, K.W.; Grima, J.N. Magnetocaloric materials with ultra-small magnetic nanoparticles working at room temperature. *Sci. Rep.* **2019**, *9*, 17607. [[CrossRef](#)] [[PubMed](#)]
32. Atanasov, R.; Bortnic, R.; Hirian, R.; Covaci, E.; Frentiu, T.; Popa, F.; Deac, I.G. Magnetic and Magnetocaloric Properties of Nano- and Polycrystalline Manganites  $\text{La}_{(0.7-x)}\text{Eu}_x\text{Ba}_{0.3}\text{MnO}_3$ . *Materials* **2022**, *15*, 7645. [[CrossRef](#)] [[PubMed](#)]
33. Wójcik, A.; Maziarz, W.; Szczerba, M.; Kowalczyk, M.; Cesari, E.; Dutkiewicz, J. Structure and inverse magnetocaloric effect in Ni-Co-Mn-Sn(Si) Heusler alloys. *Intermetallics* **2018**, *100*, 88–94. [[CrossRef](#)]
34. Bachaga, T.; Zhang, J.; Ali, S.; Suñol, J.J.; Khitouni, M. Impact of annealing on martensitic transformation of  $\text{Mn}_{50}\text{Ni}_{42.5}\text{Sn}_{7.5}$  shape memory alloy. *Appl. Phys. A* **2019**, *125*, 146. [[CrossRef](#)]
35. Żuberek, R.; Chumak, O.M.; Nabiałek, A.; Chojnacki, M.; Radelytskyi, I.; Szymczak, H. Magnetocaloric effect and magnetoelastic properties of NiMnGa and NiMnSn Heusler alloy thin films. *J. Alloys Compd.* **2018**, *748*, 1–5. [[CrossRef](#)]
36. Sun, H.; Jing, C.; Zeng, H.; Su, Y.; Yang, S.; Zhang, Y.; Bachaga, T.; Zhou, T.; Hou, L.; Ren, W. Martensitic Transformation, Magnetic and Mechanical Characteristics in Unidirectional Ni–Mn–Sn Heusler Alloy. *Magnetochemistry* **2022**, *8*, 136. [[CrossRef](#)]
37. Sofronie, M.; Popescu, B.; Enculescu, M.; Tolea, M.; Tolea, F. Processing Effects on the Martensitic Transformation and Related Properties in the  $\text{Ni}_{55}\text{Fe}_{18}\text{Nd}_2\text{Ga}_{25}$  Ferromagnetic Shape Memory Alloy. *Nanomaterials* **2022**, *12*, 3667. [[CrossRef](#)] [[PubMed](#)]
38. Czaja, P.; Wróblewski, R.; Grzonka, J.; Przewoźnik, J.; Maziarz, W. Microstructure, Martensitic Transformation, and Inverse Magnetocaloric Effect in  $\text{Ni}_{48}\text{Mn}_{39.5}\text{Sn}_{12.5-x}\text{Al}_x$  Metamagnetic Shape Memory Alloys. *Magnetochemistry* **2018**, *4*, 19. [[CrossRef](#)]
39. Höglin, V.; Cedervall, J.; Andersson, M.S.; Sarkar, T.; Hudl, M.; Nordblad, P.; Andersson, Y.; Sahlberg, M. Phase diagram, structures and magnetism of the  $\text{FeMnP}_{1-x}\text{Six}$ -system. *RSC Adv.* **2015**, *5*, 8278. [[CrossRef](#)]
40. Yu, H.Y.; Zhu, Z.R.; Lai, J.W.; Zheng, Z.G.; Zeng, D.C.; Zhang, J.L. Enhance magnetocaloric effects in  $\text{Mn}_{1.15}\text{Fe}_{0.85}\text{P}_{0.52}\text{Si}_{0.45}\text{B}_{0.03}$  alloy achieved by copper-mould casting and annealing treatments. *J. Alloys Compd.* **2015**, *649*, 1043–1047. [[CrossRef](#)]
41. He, A.; Svitlyk, V.; Mozharivskyj, Y. Synthetic Approach for  $(\text{Mn,Fe})_2(\text{Si,P})$  Magnetocaloric Materials: Purity, Structural, Magnetic, and Magnetocaloric Properties. *Inorg. Chem.* **2017**, *56*, 2827–2833. [[CrossRef](#)] [[PubMed](#)]
42. Ou, Z.Q.; Zhang, L.; Dung, N.H.; van Eijck, L.; Mulders, A.M.; Avdeev, M.; van Dijk, N.H.; Brück, E. Neutron diffraction study on the magnetic structure of Fe<sub>2</sub>P-based  $\text{Mn}_{0.66}\text{Fe}_{1.29}\text{P}_{1-x}\text{Si}_x$  melt-spun ribbons. *J. Mag. Mag. Mater.* **2013**, *340*, 80–85. [[CrossRef](#)]

43. Bao, L.L.; Meijuan, W.; Yibole, H.; Ou, Z.Q.; Guillou, F. Magnetization steps at the ferromagnetic transition of  $(\text{Mn,Fe})_2(\text{P,Si})$  single crystals. *J. Alloys Compd.* **2024**, *970*, 172612. [[CrossRef](#)]
44. Xu, J.Y.; Guillou, F.; Yibole, H.; Hardy, V. Peltier cell calorimetry “as an option” for commonplace cryostats: Application to the case of  $\text{MnFe}(\text{P,Si,B})$  magnetocaloric materials. *Fundam. Res.* **2022**, *in press*. [[CrossRef](#)]
45. Thang, N.V.; Yibole, H.; van Dijk, N.H.; Brück, E. Effect of heat treatment conditions on  $\text{MnFe}(\text{P,Si,B})$  compounds for room-temperature magnetic refrigeration. *J. Alloys Compd.* **2017**, *699*, 633–637. [[CrossRef](#)]
46. Jing-Ting, Z.; Yibole, H.; Tegus, O. The influence of preparation process on the magnetic and magnetocaloric effects of  $(\text{Mn,Fe})_2(\text{P,X})$  ( $\text{X} = \text{Ge,Si,B}$ ) compounds. *J. Inner Mongolia Normal Univ. (Nat. Sci. Ed.)* **2021**, *50*, 197–203. (In Chinese)
47. Guillou, F.; Sun-Liting; Haschuluu, O.; Ou, Z.Q.; Brück, E.; Tegus, O.; Yibole, H. Room temperature magnetic anisotropy in  $\text{Fe}_2\text{P}$ -type transition metal based alloys. *J. Alloys Compd.* **2019**, *800*, 403–411. [[CrossRef](#)]
48. Rodríguez-Carvajal, J. Recent advances in magnetic structure determination by neutron powder diffraction. *Phys. B Condens. Matter* **1993**, *192*, 55–69. [[CrossRef](#)]
49. Sosa, J.M.; Huber, D.E.; Welk, B.; Fraser, H.L. Development and application of MIPAR™: A novel software package for two-and three-dimensional microstructural characterization. *Integr. Mater. Manuf. Innov.* **2014**, *3*, 10. [[CrossRef](#)]
50. Carvalho, A.M.G.; Coelho, A.A.; von Ranke, P.J.; Alves, C.S. The isothermal variation of the entropy ( $\Delta S_T$ ) may be miscalculated from magnetization isotherms in some cases:  $\text{MnAs}$  and  $\text{Gd}_5\text{Ge}_2\text{Si}_2$  compounds as examples. *J. Alloys Compd.* **2011**, *509*, 3452–3456. [[CrossRef](#)]
51. Sandeman, K.G. Magnetocaloric materials: The search for new systems. *Scr. Mater.* **2012**, *67*, 566–571. [[CrossRef](#)]
52. Porcari, G.; Fabbri, S.; Pernechele, C.; Albertini, F.; Buzzzi, M.; Paoluzi, A.; Kamarad, J.; Arnold, Z.; Solzi, M. Reverse magnetostructural transformation and adiabatic temperature change in Co- and In-substituted Ni-Mn-Ga alloys. *Phys. Rev. B* **2012**, *85*, 024414. [[CrossRef](#)]
53. Guillou, F.; Yibole, H.; Kamantsev, A.; Porcari, G.; Cwik, J.; Koledov, V.; van Dijk, N.H.; Brück, E. Field dependence of the magnetocaloric effect in  $\text{MnFe}(\text{P,Si})$  materials. *IEEE Trans. Magn.* **2015**, *51*, 2503904. [[CrossRef](#)]
54. Verlinden, B.; Driver, J.; Samajdar, I.; Doherty, R.D. *Thermo-Mechanical Processing of Metallic Materials*, 1st ed.; Cahn, R.W., Ed.; Pergamon Materials Series; Elsevier: Amsterdam, The Netherlands, 2007.
55. Suye, B.; Yibole, H.; Meijuan, W.; Wurentuya, B.; Guillou, F. Influence of the particle size on a  $\text{MnFe}(\text{P,Si,B})$  compound with giant magnetocaloric effect. *AIP Adv.* **2023**, *13*, 025203. [[CrossRef](#)]

**Disclaimer/Publisher’s Note:** The statements, opinions and data contained in all publications are solely those of the individual author(s) and contributor(s) and not of MDPI and/or the editor(s). MDPI and/or the editor(s) disclaim responsibility for any injury to people or property resulting from any ideas, methods, instructions or products referred to in the content.